Numerical Simulation of Metal Defect Detection Based on Laser Ultrasound

Yuhe Wang , Shiwei Han, Yang Yu, Xuan Qi, Yuqin Zhang , Yudong Lian , Zhenxu Bai, Yulei Wang, and Zhiwei Lv

Abstract—The noncontact and wide-band characteristics of the ultrasonic signal excited by the laser make it widely used in nondestructive detection. In this paper, the finite element method is used to simulate multiple ultrasonic signal modes and the responses of them to metal defects. The simulation shows that the changes of excited Rayleigh-wave (RW) and shear-wave (SW) can be used to research the surface crack and internal defect of the sample respectively. By analyzing the reflected wave of RW and SW at the inspection point, the effects of surface crack and internal defect on the ultrasonic signals of the two modes are quantitatively compared. The results show that the time delay of the Rayleigh echo has a linear relationship to the width and transverse position of the crack, and the peak-valley difference of Rayleigh echo at the inspection point and the crack depth can also be fitted linearly. In addition, the Y component displacement of the bottom reflected SW also decays with the change of the internal defect. This simulation model provides a theoretical basis for further experimental verification basis.

Index Terms—Laser ultrasound, finite element, defect detection, Rayleigh-wave, shear-wave.

I. INTRODUCTION

THE commonly used defect detection techniques include eddy current, magnetic particle, penetration, X-ray and laser ultrasonic detection. The first several detection technologies have complex processes, narrow application scope, and need to be in close contact with materials. Laser ultrasonic detection has the advantages of non-contact, wide frequency band, good real-time performance and high resolution, and is

Yuhe Wang, Shiwei Han, Yang Yu, Xuan Qi, and Yuqin Zhang are with the Center for Advanced Laser Technology, Hebei University of Technology, Tianjin 300401, China, and also with the Hebei Key Laboratory of Advanced Laser Technology and Equipment, Tianjin 300401, China (e-mail: 876987202@qq.com; 192926929@qq.com; 626610316@qq.com; 1287881879@qq.com; 15033605041@163.com).

Yudong Lian, Zhenxu Bai, Yulei Wang, and Zhiwei Lv are with the Center for Advanced Laser Technology, Hebei University of Technology, Tianjin 300401, China, with the Hebei Key Laboratory of Advanced Laser Technology and Equipment, Tianjin 300401, China, and also with the Tianjin Key Laboratory of Electronic Materials and Devices, Tianjin 300401, China (e-mail: ydlian@hebut.edu.cn; zxbai@hebut.edu.cn; wyl@hebut.edu.cn; zhiweilv@hebut.edu.cn).

Digital Object Identifier 10.1109/JPHOT.2021.3097997

suitable for long-distance detection or online detection under harsh environment [1]. Laser ultrasound technology involves optics, acoustics, electricity and materials science, which is a new interdisciplinary subject formed by the combination of ultrasound and laser technology [2]–[12]. Laser ultrasonic detection has broad application prospects, and it is of great significance to improve the safety and stability of structures by applying it to aerospace, precision instruments, special materials and other fields.

Simulating the thermal coupling of the system is an important part of the detection process, which is based on the theory of thermoelasticity. When the laser incidents on the sample, the material surface absorbs light energy to cause thermal expansion, and then excite the ultrasonic signals of different modes such as Rayleigh-wave (RW), shear-wave (SW), longitudinal-wave (LW). Based on the finite element method, Dai *et al*. [13] established the transient displacement field model of the surface grooving at different depths and azimuths and evaluated the position of the kerf by reflected RW. Wang *et al*. [14] established the finite element model of the coated substrate, and obtained the transient temperature field and temperature gradient field under the condition of considering the dependence of material characteristics on temperature. Some literatures [15], [16] have analyzed the relationship between defect depth and surface wave parameters, such as amplitude and center frequency. Watanabe *et al*. [17] used the finite difference time domain (FDTD) method to simulate the propagation of elastic waves. In the FDTD, the influence of the edge reflection of the sample on the elastic wave is fully considered, and the critical pressure of the coating with different thickness are obtained. Wang *et al*. [18] fitted the time ratio between the forward peak of the Rayleigh echo and the next maximum forward displacement with the surface crack depth. The linear fitting relationship provided a method for the measurement of the surface crack depth, but the reason for fitting the time ratio is not given. At present, most of the simulations based on laser ultrasonic detection are the qualitative analysis for a specific defect [19]–[21]. There are few studies that systematically discuss the detection process and make the fitting quantitative analysis of the results.

This paper established a two-dimensional model of the cross-section of the material, and numerically simulates the effect of surface crack and internal defect on the laser ultrasonic signal of aluminum samples. The relationship between the peak-valley amplitude difference and arrival delay of the Rayleigh echo at
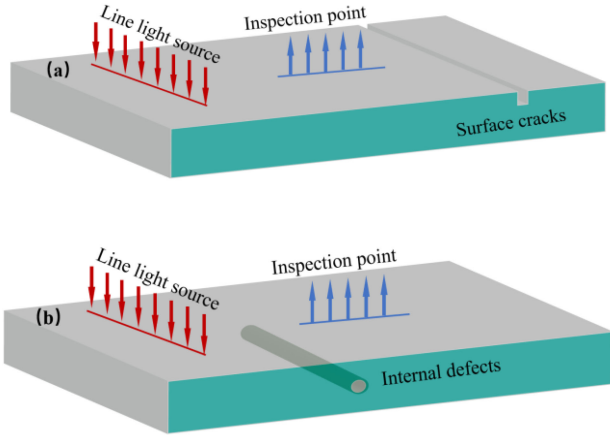
Fig. 1. Schematic diagram of the ultrasonic signal generated by the laser. (a) surface crack sample; (b) internal defect sample.

Fig. 2. Gaussian excitation pulse.

the inspection point and the changes of the width, depth and transverse position of the surface crack are analyzed. The influences of the diameter and position of the internal circular defect on the reflected SW at the inspection point are summarized. In addition, the linear equation and mean square error (MSE) are given by data fitting for surface crack detection, and the average fitting similarity exceeds 98.5%.

II. THEORETICAL BASIS AND SIMULATION MODEL

A. Generation of Laser Ultrasound by Thermoelastic Theory

The ultrasonic signals generated by laser line source are shown in Fig. 1. Laser generated ultrasonic signal can be divided into ablation mechanism and thermoelastic mechanism. When the peak power density exceeds 10^7W/cm^2, the plasma moves vertically upward on the sample surface due to pulse irradiation. According to the principle of force interaction, there are elastic stress and tangential stress perpendicular to the sample, and the distribution of elastic force is related to the ablation range of laser irradiation. When the peak power density is less than 10^7W/cm^2, the pulse irradiates on the sample, one part is reflected by the sample or absorbed by the air, and the other part acts on the surface of the sample. Because the heat concentration is too fast to release, the transient elastic stress distribution appears on the surface of the specimen, which shows the local thermal expansion of the specimen surface. In the near-field region, the stress distribution is hindered by the structure of the sample which is not affected by the temperature, while the far-field stress distribution is mainly determined by the thermoelastic stress relationship of the sample material.

The heat conduction equation (Cylindrical Coordinate) based on the isotropic media can be described as:

$$\rho C_V \frac{\partial T(r,z,t)}{\partial t} = \frac{1}{r}\frac{\partial}{\partial r}\left(rk\frac{\partial T(r,z,t)}{\partial r}\right) + \frac{\partial}{\partial z}\left(k\frac{\partial T(r,z,t)}{\partial z}\right) \tag{1}$$

Where ρ, C_V, and k respectively represent the constant pressure heat capacity, density and thermal conductivity of the material; $T(r, z, t)$ is the temperature distribution function. The energy
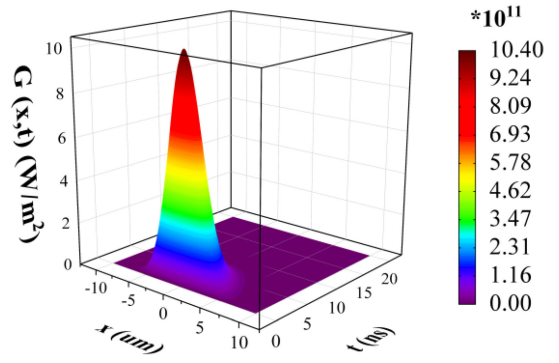
transfer inside the material is completed in the form of heat conduction. The influence of thermal convection and radiation on temperature variation can be ignored, and it can be regarded as only applying a single boundary heat source on the upper surface. Since the spot range is much smaller than the sample size, the side surface of the sample meets the thermal insulation conditions. The boundary conditions of thermoelastic theory can be described as:

$$-k\left.\frac{\partial T(r,z,t)}{\partial z}\right|_{z=d_1} = G = I_0 f(x)g(t) \tag{2}$$

$$\left.\frac{\partial T(r,z,t)}{\partial z}\right|_{z=d_2} = \left.\frac{\partial T(r,z,t)}{\partial r}\right|_{r=R} = 0 \tag{3}$$

Where d_1 and d_2 are the upper and lower boundary dimensions of the model, R represents the side boundary, G is the heat source density, and I_0 is the laser peak power density. The space and time distribution functions of the pulse are expressed as:

$$f(x) = exp\left(-(x-x_0)^2/R_0^2\right) \tag{4}$$

$$g(t) = \frac{t}{t_0}*exp\left(-\frac{t}{t_0}\right) \tag{5}$$

Where x_0 is the abscissa of the pulse action point, R_0 is the spot radius, and t_0 is the pulse width. The Gaussian excitation pulse is shown in Fig. 2. The temperature changes of each point in the material can be obtained by combining the three equations (1), (2), (3).

The existence of thermal expansion causes a slight displacement on the surface. The governing equation and bottom boundary condition of the structural mechanics are expressed as:

$$(\lambda + \mu)\nabla(\nabla \cdot U) + \mu\nabla \times \nabla \times U$$
$$- \alpha_T(3\lambda + 2\mu)\nabla T = \rho\frac{\partial^2 U}{\partial^2 t} \tag{6}$$

$$n \cdot [\sigma - (3\lambda + 2\mu)\alpha_T\nabla T(r,z,t)I]|_{d_2} = 0 \tag{7}$$

In the formula, U is the displacement field, λ and μ are Lamb constants, α_T is the thermal expansion coefficient, and n is the unit vector perpendicular to the surface. In addition, the initial displacement of the sample is set to 0, that is $U(r,z,t)|_{t=0} = \frac{\partial U(r,z,t)}{\partial t}|_{t=0} = 0$.
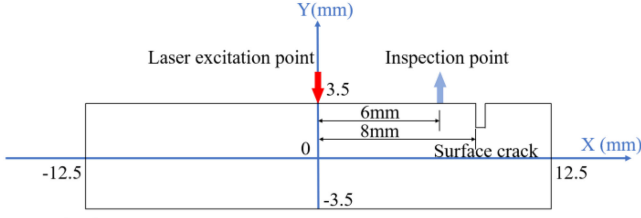
Fig. 3.   Surface crack detection model.

Fig. 4.   Internal defect detection model.

B. Finite Element Method

When using the finite element method for thermal analysis, the heat conduction equation can be expressed as:

$$[K]\{T\} + [C]\{\dot{T}\} = \{P_1\} + \{P_2\} \qquad (8)$$

Where $[K]$ is the heat conduction matrix, $[C]$ is the sample heat capacity matrix, $\{T\}$ is the temperature, $\{\dot{T}\}$ is the temperature change rate, and are the heat flux vector and the heat source vector matrix respectively. Ignoring the ultrasonic attenuation, the finite element form of the linear thermoelastic equation is:

$$[M]\{\ddot{U}\} + [K]\{U\} = \{F_{ext}\} \qquad (9)$$

Where $[M]$ is the sample mass matrix, $[K]$ is the stiffness matrix, $\{\ddot{U}\}$ is the vector acceleration, $\{U\}$ is the displacement vector, and $\{F_{ext}\}$ is the laser action vector. Solving the formula by time integration method, and set the time step to Δt. Displacement and the first derivative at time $t+\Delta t$ are expressed as:

$$\{U\}_t + [(1-\theta)\{U\}_t + \theta\{U\}_{t+\Delta t}]\Delta t = \{U\}_{t+\Delta t} \qquad (10)$$

$$\{U\}_t + \Delta t\{U\}_t + [(0.5-\gamma)\{U\}_t + \gamma\{U\}_{t+\Delta t}]\Delta t^2$$
$$= \{U\}_{t+\Delta t} \qquad (11)$$

θ and γ are parameters that control the integral accuracy and stability respectively, and the displacement curve within the action time can be obtained by solving the integral.

C. Model Establishment and Parameter Setting

In this paper, the two-dimensional cross-section of an aluminum thin plate is used as a model to simulate the variation of ultrasonic signal on its surface. The surface crack detection model with size is shown in Fig. 3. Because the internal defect is detected by the reflected SW which need a bottom reflection process, the distance between the excitation and inspection point is set longer. The internal defect detection model is shown in Fig. 4.

Based on the previous theoretical foundation, the transient temperature field and stress field are numerically simulated. The exciting pulse parameters and the physical characterization parameters of aluminum material are shown in Table I and Table II respectively.
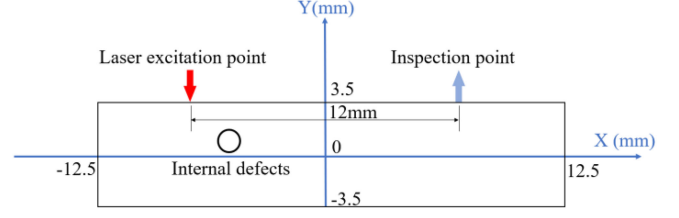
TABLE I
PARAMETER SETTING OF EXCITATION PULSE

Monopulse energy	Pulse width	Spot radius	Peak power density
1 mJ	10 ns	300 um	3.5368×10^{11} W/m^2

TABLE II
PHYSICAL PROPERTIES OF ALUMINUM IN SIMULATION MODEL

Characteristic	Aluminum
Thermal conductivity	238 W/(m*K)
Density	2700 kg/m^3
Constant pressure heat capacity	900 J/(kg*K)
Young's modulus	70×10^9 Pa
Poisson's ratio	0.33
Coefficient of thermal expansion	23×10^{-6}1/K

III. SIMULATION RESULTS AND ANALYSIS

A. Transient Temperature Field and Stress Field

Laser ultrasonic detection is a multi-physics coupling process, which involves two parts: solid heat transfer and structural mechanics. Under laser irradiation, the temperature of the sample surface rises to form a transient temperature field. The inability to release a large amount of absorbed heat in time causes the thermal expansion of the sample surface, which leads to the generation of a transient stress field. Observing the transient temperature and stress field cannot directly show the effect of defects on the ultrasonic signal, but it can be a good study of the essential causes of the ultrasonic signal. This paper is based on the overall detection process. Before analyzing the influence of sample defects on the ultrasonic signal, the above two physical processes are firstly researched. The instantaneous temperature and stress changes are also investigated.

1) Transient Temperature Field: When the laser radiates to the surface of the sample, the sample absorbs the light energy and converts it into heat energy. At the same time, the transient temperature field is formed in the range of laser action. The changes of transverse and longitudinal temperature fields are simulated, as shown in Fig. 5.

It can be seen that the closer to the laser action point (0, 3.5), the faster the temperature rises and the higher the peak value. As the distance from the laser point goes away, the temperature rises more slowly and remains flat after exceeding the heat conduction distance of the sample. During the exciting process, the transient temperature field only exists in a small range near the surface (transverse: 12 um, longitudinal: 6 um), which is related to the
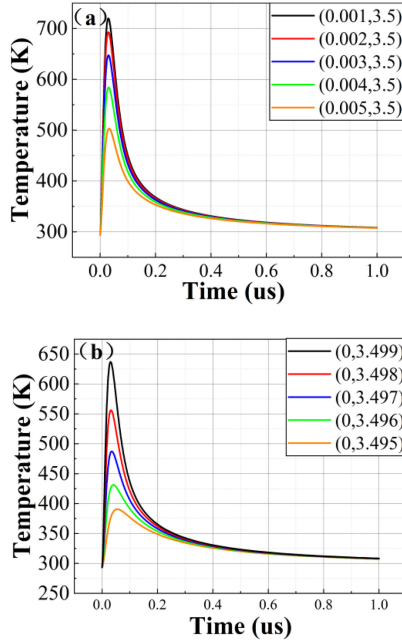
Fig. 5.   Transient temperature field at different points. (a) transverse temperature field changes; (b) longitudinal temperature field changes.
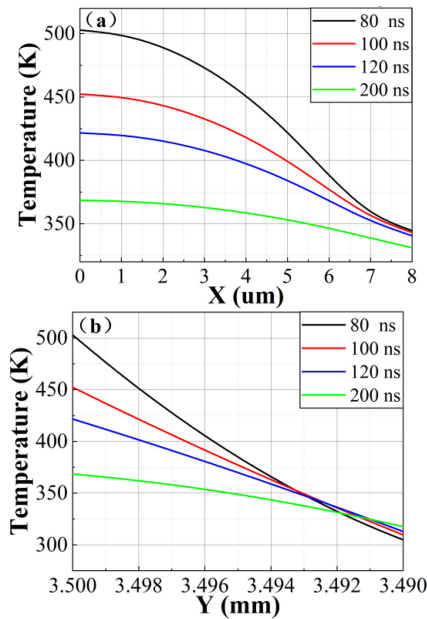

Fig. 6.   Temperature field changes at different times. (a) the change of horizontal temperature field; (b) the change of longitudinal temperature field.
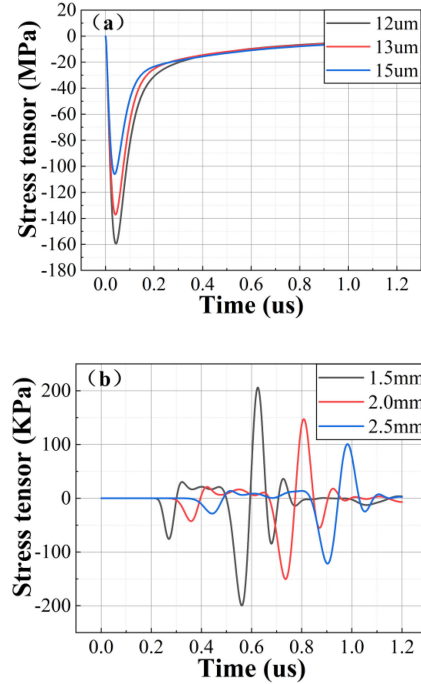

Fig. 7.   Stress tensor of laser line source at different transverse distances. (a) near-field stress tensor; (b) far-field stress tensor.

a downward trend. After a period of time, due to the conduction of the surface temperature to the inside, the internal temperature of the sample may be higher than the surface temperature.

2) Transient Temperature Field: Under the thermoelastic mechanism, the nonuniformly distributed temperature field causes different degrees of deformation of the sample surface, which is the result of transient stress. Fig. 7 shows the variation of the stress tensor with time at different lengths (transverse) from the laser line source. The stress in the laser irradiation area is determined by the temperature field, while the stress far away from the laser irradiation area is determined by the propagation of elastic acoustic wave in the material. Therefore, the area which not affected by the temperature will hinder the thermal expansion of the heating area, and a horizontal positive compressive stress will appear on the surface of the material, resulting in a negative maximum of the horizontal stress tensor in the laser irradiation near-field area, as shown in Fig. 7(a). The irradiated far-field area is little affected by temperature, and its stress field is mainly determined by the thermoelastic stress relationship and can reflect the propagation characteristics of ultrasonic waves, as shown in Fig. 7(b).

In the same way, the variations of the stress tensor with time in different length (longitudinal) from the laser line source are simulated. The longitudinal near-field region is affected by the temperature transfer and will release thermal expansion in both the inner and outer directions, resulting in the positive and negative extreme values of its stress tensor, as shown in Fig. 8(a). The stress waveform in the far-field region characterizes the ultrasonic signal, and its amplitude is also smaller than that in the near-field region of thermal action, as shown in Fig. 8(b).
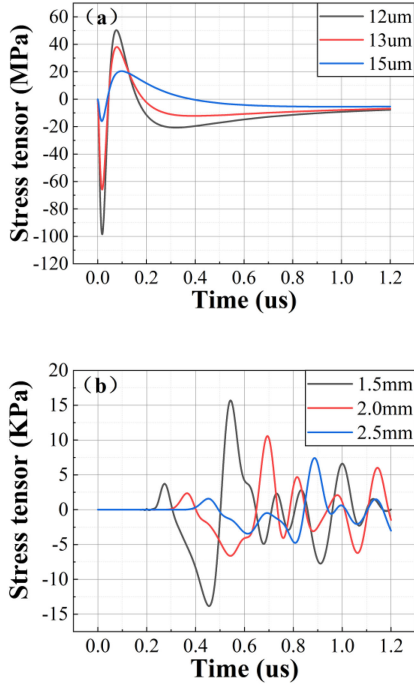
setting of the distribution function of the Gaussian pulse. The transverse and longitudinal distributions of temperature field at different time are shown in Fig. 6.

It can be observed that the transverse distribution of the temperature field is determined by the spatial distribution of the excitation pulse, which has obvious Gaussian distribution characteristics and decreases with time. The longitudinal distribution of the temperature field at different times is determined by the thermal conductivity of the aluminum sample and shows

Fig. 8. The stress tensor of the laser line source at different longitudinal distances. (a) near-field stress tensor; (b) far-field stress tensor.
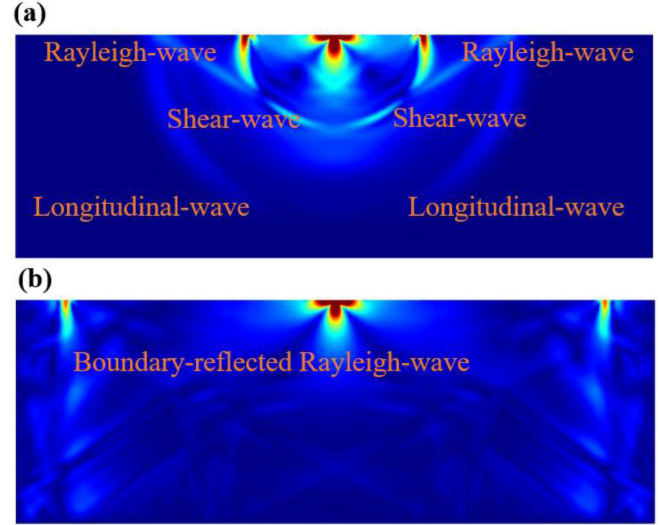

Fig. 9. Ultrasonic signals of the complete sample at different times. (a) 1.0us; (b) 4.0us.

Fig. 10. Ultrasonic signals of surface crack samples at different times. (a) 3.5us; (b) 4.0us.

3) Laser Generates Ultrasonic Signal

The thermal expansion stress generated by the transient temperature field is the excitation source of ultrasonic signal, and a variety of ultrasonic signals are excited on the sample surface, including RW, SW and LW. When the sample is in good condition, RW propagates along the surface of the sample to both sides of the boundary, and forms a boundary-reflected Rayleigh-wave (BRW) after reflection. LW radiates in the form of a single cultivar on both sides of the normal line, and the maximum amplitude appears at an angle of 60°; SW radiates in the form of double cultivar on both sides of the normal line, the main lobe amplitude is the largest at an angle of 30°, and the overall included angle ranges from 30° to 45°. The simulation results of ultrasonic signals are shown in Fig. 9.

When a crack appears on the surface, the RW propagates along the surface is affected by the crack and appears three situations: (i) a part is reflected by the left edge of the crack to form a crack-reflected Rayleigh-wave (CRW); (ii) a part propagates down along the crack contour to form mode conversion longitudinal-wave (MLD) and mode conversion shear-wave (MSW); (iii) the rest is transmitted through the crack to form a transmitted Rayleigh-wave (TRW) and reflected by the right boundary. The simulation results are shown in Fig. 10.

For the detection of internal defect, this paper mainly observes the changes of the SW signal. SW propagates in a nondestructive sample and will reflect multiple times on the upper and lower boundaries of the sample until they are absorbed inside the sample. When there is a defect in the sample, the defect in the propagation path of the SW will directly affect its intensity. In

Fig. 11, it can be observed that the intensity of the bottom-reflected shear-wave (BSW) gradually changes from bright to dim. Part of this change in brightness is caused by the absorption of the material, but the barrier of defects is the main reason.

B. Surface Crack Detection

Effects of Surface crack's width, depth and transverse position on ultrasonic signals are simulated and analyzed. Without special explanation, parameters are set as follows: depth is 0.2 mm, width is 0.2 mm, transverse position is 8 mm.

1) Crack Width Detection: Crack depth is controlled as 0.2 mm, the width is increased from 0.1 mm to 0.5 mm, and the distance between the excitation and the inspection point is 6 mm. Under different widths, the Y component displacement changes are shown in Fig. 12.
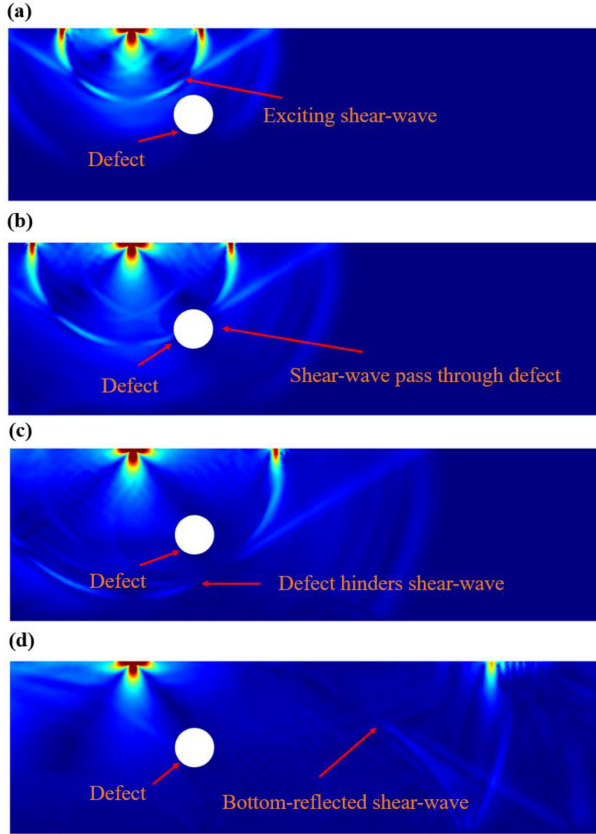
Fig. 11. Ultrasonic signals of internal defect samples at different times. (a) 1.10 us; (b) 1.40 us; (c) 2.00 us; (c) 5.00 us.
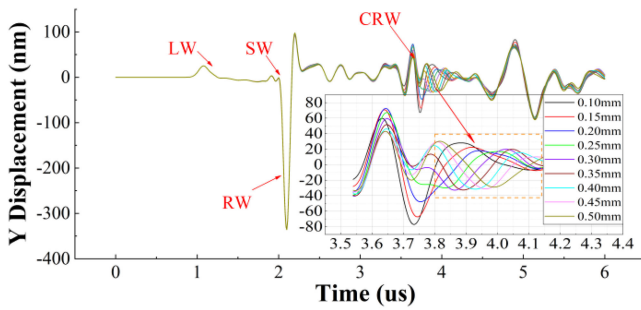

Fig. 12. Y component displacement of ultrasonic signal under different widths.

For the same inspection point, the main part of the CRW arrives at almost the same time, and its "tail" has different degrees of time delay. The analysis shows that the CRW is not simply reflected by the left boundary of the crack, and a small distance from the bottom edge of the crack will also reflect the Rayleigh signal, and this distance is positively correlated with the crack width. Accordingly, we performed data fitting for time delay and width variation, and the results are shown in Fig. 13.

According to the analysis of fitting data, the linear relationship can be expressed as:
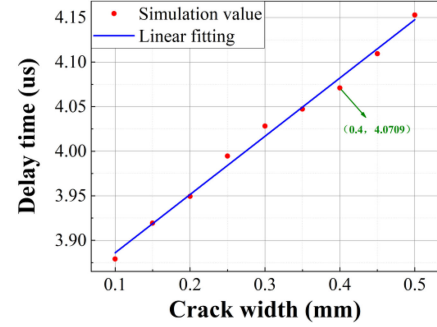
$$T_1 = 0.6531x_1 + 3.8207 \tag{12}$$

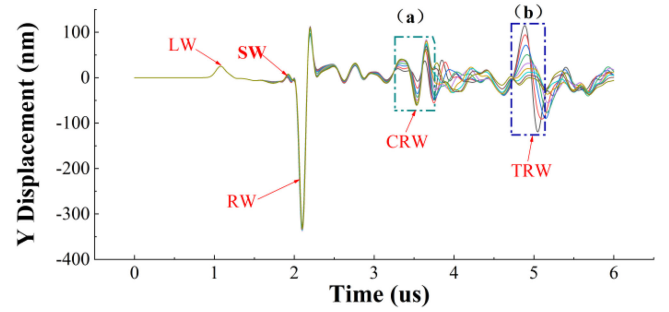Fig. 13. Fitting relationship between time delay and crack width.

Fig. 14. Y component displacement of ultrasonic signal under different depths.

Where T_1 is the time when CRW arrives at inspection point, and x_1 represents the crack width change. Taking the farthest points (0.4, 4.0709) from the fitting line, the fitting error can be calculated to be 0.27%, and the overall root mean square error (RMSE) is 0.00831. It can be seen that there is an approximate linear relationship between the delay time and the corresponding width, and the correlation coefficient R reaches 99.57%. The crack width can be approximated by observing the CRW's delay time.

2) Crack Depth Detection: The crack width was controlled as 0.2mm, the crack depth increased from 0.1 mm to 0.5 mm, and the distance between the excitation point and the inspection point unchanged. The Y component displacements are shown in Fig. 14. Ultrasonic signals at different depths are basically consistent, except for the opposite variation of displacement amplitude at a and b.

In Fig. 15, the amplification of the two signals shows that with the crack depth increasing, the displacement of CRW 's Y component (a) gradually increases, while the displacement of TRW's Y component (b) reflected by the right boundary gradually decreases. When the crack depth reaches the ultrasonic wavelength, Rayleigh signal will be completely reflected by the crack.

The displacement of CRW at T = 3.54 us and that of TRW at T = 4.89 us were extracted respectively, and the displacement changes of Y component at two specific moments were fitted to the crack depth, as shown in Fig. 16(a).

It can be seen that simply using displacement changes cannot linearly express the depth influence. Therefore, the peak-valley displacement difference of the TRW reflected by the
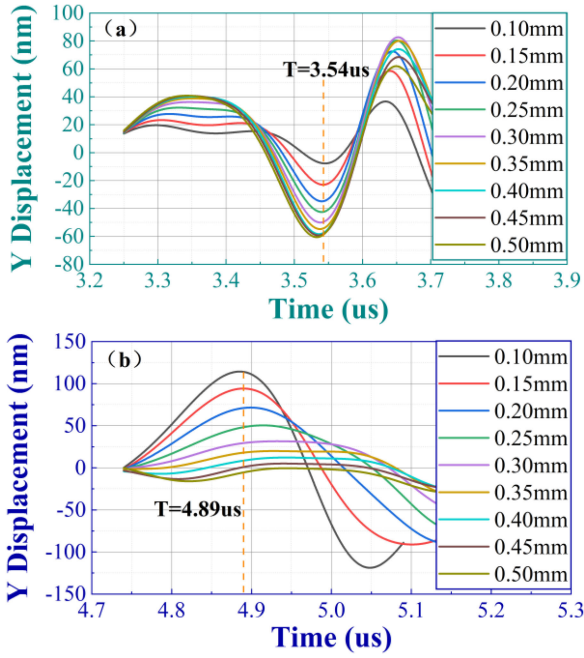
Fig. 15. Y component displacement of Rayleigh signal. (a) CRW; (b) TRW.

right boundary is used for fitting, which has an obvious linear relationship with the crack depth, as shown in Fig. 16(b). The linear relationship expression is:

$$\Delta Y = -545.2386k + 251.6982 \tag{13}$$

ΔY is the peak-valley displacement difference, and k represents the change in crack depth. Taking the farthest point from the fitting line (0.35, 86.8939), the fitting error can be calculated to be 0.66%, and the RMSE is 10.643. Compared with the crack width fitting, the linear fitting of the depth using the peak-valley displacement difference will cause a certain deviation due to the loss of the ultrasonic signal intensity by the sample. However, it can still be observed that there is a linear relationship between the peak-valley difference and the corresponding depth change, and the correlation coefficient R reaches 98.94%.

3) Changes in the Transverse Position of Cracks: For the crack fixed in a certain position, the change of width will delay the time of CRW's tail reaches the detection point, and the change of depth will affect the displacement amplitude of Y component of TRW. For cracks with transverse position changes, the distance between the crack and the inspection point is increased from 1.5 mm to 2.5 mm in this paper, and the results are shown in Fig. 17.

As crack moves to the right boundary, the time of CRW arrives at the inspection point is delayed, which is consistent with the propagation characteristics of ultrasonic signal. According to this, the delay time and the position changes are fitted, which is shown in Fig. 18. It is the same as the linear fitting of width and depth, the linear relation between them is expressed as follows:
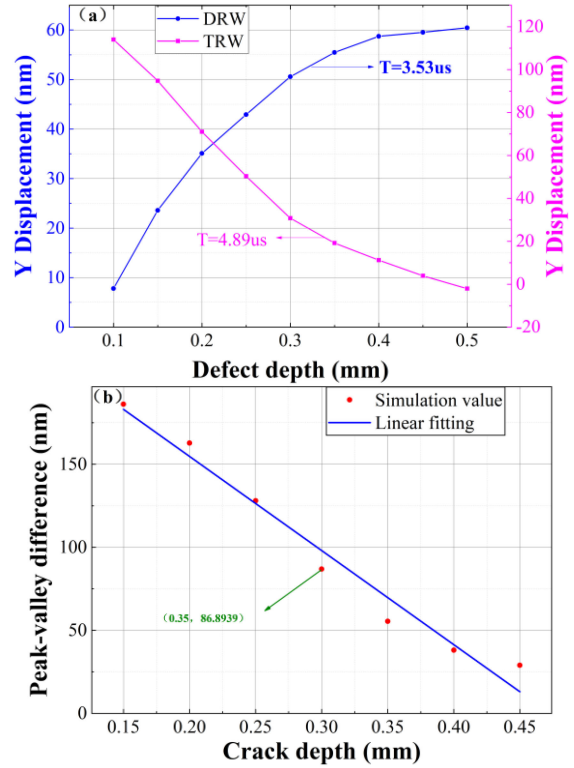
$$T_2 = 0.6862x_2 + 2.2769 \tag{14}$$

Fig. 16. Data fitting results of different ultrasound signals. (a) the displacement changes of the CRW AND TRW; (b) the peak-valley displacement difference of the TRW reflected by right boundary.
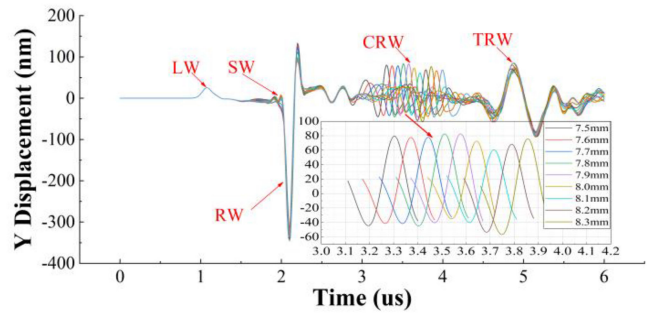

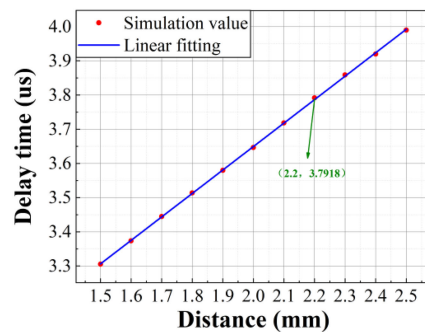Fig. 17. Y component displacement changes at different crack positions.

Fig. 18. Fitting relationship between delay time and crack transverse position.
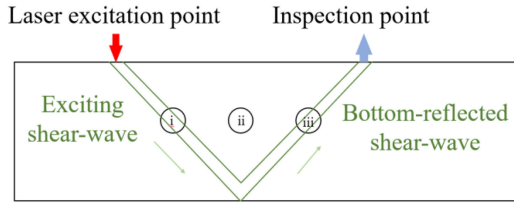
Fig. 19   The diagram of Shear-wave propagation path.

T_2 is the delay time and x_2 is the change range of crack position. Taking the relative far points (2.2, 3.7918), the maximum fitting error is 0.13%, the total RMSE is 0.0029, and the final linear fitting coefficient R reaches 99.99%, which indicates that the crack transverse axis position can be expressed linearly by the delay time.

C. Internal Defect Detection

The internal defects are simulated and analyzed from the three aspects of transverse change, longitudinal change and radius size, and the influences of three factors on the ultrasonic signal are discussed.

1) Defect Transversal Position Detection: During the actual inspection process, the specific location of the defect is not known, so the sample will be dynamically inspected by scanning [22]. In the simulation, the distance between the excitation and the detection point is 12mm, and the scanning process is simulated by changing the abscissa of the center of the internal defect. In the process of moving, the SW signal will appear in three situations due to the different position of the defect: (i) the defect is on the incident path of the SW, resulting in a decrease in the amplitude of the BSW; (ii) the defect is located between the incident/reflected SW propagation path and does not affect the amplitude of BSW; (iii) the defect is on the reflected path of the BSW, causing its amplitude to decrease again. The specific situation is shown in Fig. 19.

In the simulation, the defect radius is set at 0.8mm, the ordinate of the center is 0, and the abscissa changes from -7 to 5.5. Eight groups of data are taken for analysis, as shown in Fig. 20.

As the defect moves to the right, the Y component displacement of the BSW decreases – increases - decreases again - increases again. The difference between the peak-valley value of the BSW signal at different defect positions and the peak -valley value of the BSW signal without defect is shown in Fig. 21.

The two peaks show the two changes of the BSW. This is consistent with the change trend shown in Fig. 20, which verifies the feasibility of the proposed detection method and reflects the influence of the transverse position change of internal defects on the SW signal.

2) Longitudinal Position Detection of Defects: Keeping the defect radius constant, the abscissa is fixed at 3.5, and the distance between the center of the circle and the upper surface is increased from 1.5 mm to 3.5 mm in steps of 0.5mm. The simulation result is shown in Fig. 22.
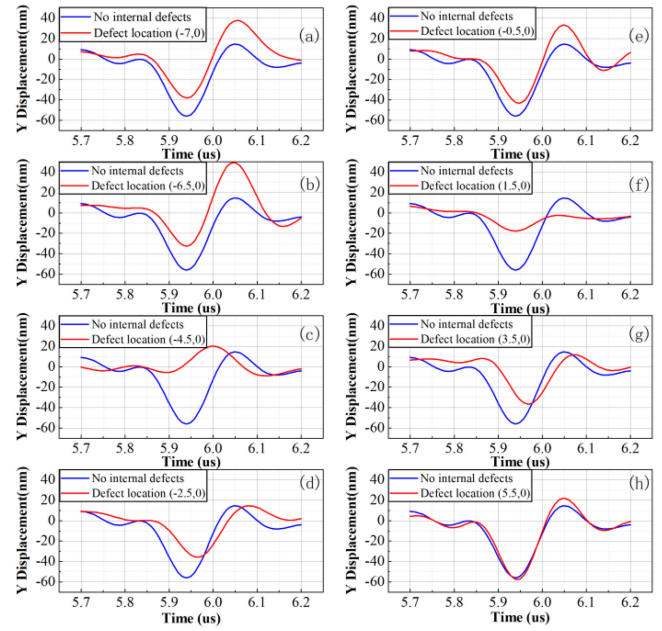

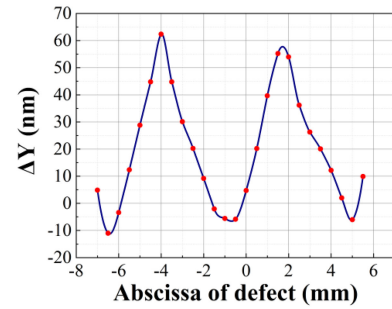Fig. 20.   Variation of Y component displacement at different defect positions.

Fig. 21.   The relationship between the lateral change of the defect and the displacement difference.
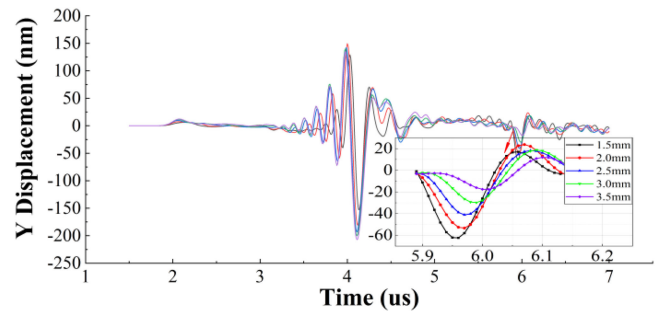

Fig. 22.   The Y component displacement changes of different depth defects.

It can be found that the downward movement process of the defect gradually obstructs the incident path of the transverse wave and causes the BSW to attenuate, which is reflected in the decrease of the Y component displacement in the Fig. 22. The coincidence of this time-domain spectrum is not as good as crack detection. This is because the different longitudinal positions of the defects change the time for the transverse wave
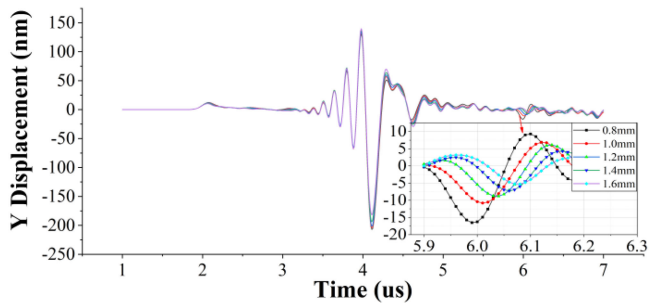
Fig. 23. Time-domain diagram of shear waves reflected from the bottom surface of defects of different sizes.

to propagate to the lower boundary of the sample, resulting in uneven distribution of BSW at the inspection point.

3) Detection of Defect Size: Finally, the effects of different sizes defects on SW are simulated. The coordinates of the center of the defect are (0, 3.5), and the radius is set to 0.8mm, 1.0mm, 1.2mm, 1.4mm, 1.6mm, and the simulation results are shown in Fig. 23.

Similar to the longitudinal changes, the increase of the defect radius hinders the propagation of the incident transverse wave, resulting in the weakening of the reflected signal intensity on the bottom surface. It can be seen from Figure 22 and Figure 23 that the peak change of BSW is the main basis for judging the existence of internal defects. The longitudinal movement of the defect gradually increases the area obstructing the propagation of the incident transverse wave, resulting in a decrease in the peak value of the reflected echo at the inspection point. As the size of the defect increases, the peak position of the reflected wave becomes smaller and smaller, which means that the larger the aperture, the more obvious the interaction between it and the transverse wave, and therefore the easier it is to detect.

4. Conclusion

In this paper, the finite element method is used to simulate the generation of laser ultrasonic signals, and the application of RW and SW ultrasonic signals in the detection of surface crack and internal defect of the sample is analyzed. The simulation results show that the time delay for the CRW signal to arrive at the same inspection point is related to the width and transverse position of the sample surface crack, the Y component displacement change of the TRW signal is related to the surface crack depth. The BSW ultrasonic signal carries the information of the internal defects of the sample, and the displacement change is related to the position and size of the defect. Through linear data fitting, the material's surface and internal damage have high similarity with the corresponding ultrasonic signal change information, and the linear fitting degree exceeds 98.5%. This article provides an analysis scheme for laser ultrasound to determine the damage location.

References

[1] D. Liu, "Research of the laser ultrasonic excitation and detection technology," Tai Yuan: North University of China, 2015.

[2] A. Kravcov *et al.*, "Laser-ultrasonic testing of the structure and properties of concrete and carbon fiber-reinforced plastics," *Key Eng. Mater.*, vol. 722, pp. 267–272, 2016.

[3] B. Zhang *et al.*, "An ultrasonic non-destructive testing method for the measurement of weld width in laser welding of stainless steel," *AIP Conf. Proc.*, vol. 1890, no. 1, pp. 1–4, 2017.

[4] X. H. Luo *et al.*, "Design and implementation of laser ultrasonic testing system based on coherent detection," *Laser Infrared.*, vol. 47, no. 11, pp. 1339–1342, Nov. 2017.

[5] Z. Zhou., "New progress of the study and application of advanced ultrasonic testing technology," *J. Mech. Eng.*, vol. 53, no. 22, pp. 1–10, Nov. 2017.

[6] J. B Xia *et al.*, "Non-contact laser ultrasonic testing of stell-plumbum bonding structure," *Infrared Laser Eng.*, vol. 47, no. 1, Jan. 2018, Art. no. 117006.

[7] D. C. Yi *et al.*, "Inspection of cracks with focused angle beam laser ultrasonic wave," *Appl. Acoust.*, vol. 145, pp. 1–6, Feb. 2019.

[8] H. Selim *et al.*, "Defect reconstruction by non-destructive testing with laser induced ultrasonic detection," *Ultrasonics*, vol. 101, Feb. 2020, Art. no. 106000.

[9] C. X. Pei *et al.*, "Fully noncontact measurement of inner cracks in thick specimen with fiber-phased-array laser ultrasonic technique," *NDT E Int.*, vol. 113, Jul. 2020, Art. no. 102273.

[10] J. C. Xiong *et al.*, "Imaging of transient surface acoustic waves by full-field photorefractive interferometry," *Rev. Sci. Instrum.*, vol. 86, no. 5, pp. 485–499, 2015.

[11] J. J. Liu *et al.*, "Weld quality inspection of small-diameter thin-walled pipes by laser ultrasonic method," *Appl. Opt.*, vol. 59, no. 12, pp. 3538–3542, Mar. 2020.

[12] I. Pelivanov *et al.*, "NDT of fiber-reinforced composites with a new fiber-optic pump–probe laser-ultrasound system," *Photoacoustics*, vol. 2, no. 2, pp. 63–74, 2014.

[13] Y. Dai *et al.*, "Finite element modeling of the interaction of laser-generated ultrasound with a surface-breaking notch in an elastic plate-ScienceDirect," *Opt. Laser Technol.*, vol. 42, no. 4, pp. 693–697, 2010.

[14] J. J. Wang *et al.*, "Numerical simulation of laser-generated surface acoustic waves in the transparent coating on a substrate by the finite element method," *Opt. Laser Technol.*, vol. 39, no. 1, pp. 21–28, Feb. 2007.

[15] H. L. Guo, B. Zheng, and H. Liu, "Numerical simulation and experimental research on interaction of micro-defects and laser ultrasonic signal," *Opt. Laser Technol.*, vol. 96, pp. 58–64, Nov. 2017.

[16] W. Zeng *et al.*, "Finite element simulation of laser-generated surface acoustic wave for identification of subsurface defects," *Optik*, vol. 207, Dec. 2020, Art. no. 163812.

[17] Y. Watanabe *et al.*, "Quantitative evaluation of adhesion quality of surface coating by using pulse laser-induced ultrasonic waves," *Surf. Coat. Technol.*, vol. 286, pp. 231–238, 2016.

[18] M. Y. Wang, Y. J. Zhou, and C. Guo, "Numerical simulation of laser ultrasonic detection of surface micro-crack depth," *Laser Technol.*, vol. 41, no. 2, pp. 178–181, Mar. 2017.

[19] W. Hassan and W. Veronesi, "Finite element analysis of Rayleigh wave interaction with finite-size, surface-breaking cracks," *Ultrasonics*, vol. 41, pp. 41–52, Jan. 2003.

[20] R. Wu *et al.*, "Laser ultrasonic depth measurement of surface cracks," *Nondestruct. Test. Technol.*, vol. 41, no. 09, pp. 24–27, 2019.

[21] J. F. Guan *et al.*, "Numerical study on depth evaluation of micro-surface crack by laser generated ultrasonic waves," *J. Test Meas. Technol.*, vol. 24, no. 1, pp. 15–21, 2010.

[22] W. Zeng *et al.*, "Finite element simulation of laser-generated ultrasonic waves for quantitative detection of internal defects in welds," *Optik*, vol. 221, Nov. 2020, Art. no. 165361.